Journal Pre-proof

Estimating the mode I through-thickness intralaminar R-curve of unidirectional carbon fibre-reinforced polymers using a micromechanics framework combined with the size effect method

L.F. Varandas, D. Dalli, G. Catalanotti, B.G. Falzon

PII: S1359-835X(22)00323-2
DOI: https://doi.org/10.1016/j.compositesa.2022.107141
Reference: JCOMA 107141

To appear in: *Composites Part A*

Received date : 17 May 2022
Revised date : 21 July 2022
Accepted date : 9 August 2022

Estimating the mode I through-thickness intralaminar R-curve of unidirectional carbon fibre-reinforced polymers using a micromechanics framework combined with the size effect method

L.F. Varandas[a,*], D. Dalli[b], G. Catalanotti[c], B.G. Falzon[d]

[a]*Bristol Composites Institute (BCI), University of Bristol, Queen's Building, University Walk, Bristol BS8 1TR, UK*
[b]*DEMec, Faculdade de Engenharia, Universidade do Porto, Rua Dr. Roberto Frias, 4200-465, Porto, Portugal*
[c]*Escola de Ciências e Tecnologia, Universidade de Évora, Colégio Luís António Verney, Rua Romão Ramalho, 59, 7000-671 Évora, Portugal*
[d]*School of Engineering, STEM College, RMIT University, GPO Box 2476, Melbourne, 3001, Victoria, Australia*

Abstract

A three-dimensional micromechanics framework is developed to estimate the mode I through-thickness intralaminar crack resistance curve of unidirectional carbon fibre-reinforced polymers. Finite element models of geometrically-scaled single edge notch tension specimens were generated. These were modelled following a combined micro-/meso-scale approach, where the region at the vicinity of the crack tip describes the microstructure of the material, while the regions far from the crack tip represent the mesoscopic linear-elastic behaviour of the composite. This work presents a novel methodology to estimate fracture properties of composite materials by combining computational micromechanics with the size effect method. The size effect law of the material, and consequently the crack resistance curve, are estimated through the numerically calculated peak stresses. In-depth parametric analyses, which are hard to conduct empirically, are undertaken, allowing for quantitative and qualitative comparisons to be successfully made with experimental and numerical observations taken from literature.

Keywords: B. Fracture toughness, C. Computational Modelling, C. Micromechanics, Size effect method

1. Introduction

The use of composite materials in the automotive and aerospace sectors necessitates the need to model and evaluate their mechanical performance under several loading scenarios, at different strain-rates, i.e. from quasi-static to high-rate loading regimes [1, 2]. The development of structural components may be hindered by limited design capabilities, high development costs, and slow production rates. The use of numerical simulation tools provides an opportunity to address these shortcomings [3, 4, 5, 6, 7]. Typical analyses of the mechanical performance of composite components make use of meso-scale (ply-level) material damage models to capture their behaviour under damage-inducing loads. However, these intralaminar damage models (e.g. [8, 9, 10]), depending on the damage mode, usually require, as an input, the corresponding steady-state

*Corresponding author
Email address: luis.varandas@bristol.ac.uk (L.F. Varandas)

fracture toughness, $\mathcal{R}_{ss}$, derived from the crack resistance curve ($\mathcal{R}$-curve) of the material, which is commonly determined experimentally. As evidenced in Figure 1, intralaminar crack propagation in unidirectional (UD) composite materials may occur in distinct manners, either promoting higher degree of matrix cracking, fibre-matrix interface debonding, and fibre bridging (cracks (i), (ii), (iii), and (iv)), or fibre breakage as a main toughening mechanism (cracks (v) and (vi)). A similar nomenclature to the one defined in this paper was used by Ref. [11]. It is postulated that a propagating intralaminar crack transverse (ii) and through-thickness (iii) to the fibres present similar damage mechanisms. This work is concerned with the determination of the mode I through-thickness intralaminar fracture toughness and corresponding $\mathcal{R}$-curve, similar to the experimental work conducted by Pinho et al. [12], in which a crack propagates in direction (iii), as shown in Figure 1.

[Figure 1 about here.]

Several experimental methods have been developed to characterise the mode I intralaminar fracture toughness of carbon fibre-reinforced polymers (CFRPs) for a crack propagating perpendicular to the fibres (cracks (v) and/or (vi) in Figure 1). These are most commonly grouped into stable and unstable crack propagation techniques. Stable crack propagation techniques involve the calculation of the fracture toughness through the measurement of a propagating crack, by tracking the crack tip location, and generally make use of the Compact Tension (CT) specimen or its variants [13, 14, 15, 16, 17] for intralaminar crack propagation. By contrast, using the size effect method proposed by Bažant [18], unstable crack propagation techniques make sole use of the peak loads of geometrically-scaled Single/Double Edge Notch Tension (SENT/DENT) specimens [19, 20, 21, 22, 23]. The peak load condition resulting from unstable crack propagation of such specimens occurs after some small value of initial propagation, before the Fracture Process Zone (FPZ) of the material can be fully developed.

Few authors have studied mode I transverse/through-thickness intralaminar crack propagation (crack (ii) or (iii) in Figure 1, respectively) using computational micromechanics [24, 25, 26, 27]. Canal et al. [24] studied the fracture behaviour of an E-glass/epoxy unidirectional laminate by means of stable 3-Point-Bend (3PB) tests. The mechanical behaviour was then simulated using a 2D micromechanics framework. They concluded that the mode I "matrix-dominated" intralaminar fracture toughness was mainly dependent on the fibre-matrix interfacial strength and toughness, while the matrix properties played a secondary role. Herráez et al. [26] developed a 2D numerical framework to analyse the mode I transverse fracture behaviour of an AS4/8552 composite using the Linear Elastic Fracture Mechanics (LEFM) displacement field. The authors used a framework that required the incremental update of the Boundary Conditions (BCs) throughout the numerical simulations and also the qualitative tracking of the position of the crack tip, which can induce subjective errors. More recently, Tan and Martínez-Panẽda [27] presented a coupled Phase field-Cohesive zone model (PF-CZM) framework to model this specific type of stable intralaminar crack growth, obtaining good quantitative and qualitative correlations with experimental results. However, they considered extremely tough fibre-matrix interfaces, more similar to the ones used when modelling interlaminar regions, compensating for other toughening mechanisms that were neglected in those models. Due to the two-dimensional formulation of the aforementioned micromechanical frameworks, the steady-state fracture toughness estimated from these models should be taken as a lower bound rather than a propagation value. Moreover, they all used simpler constitutive material models for the matrix material, when it has been shown that in order to accurately simulate the epoxy yielding behaviour, a paraboloidal yield criterion should be used [28, 29].

The "matrix-dominated" steady-state intralaminar fracture toughness is typically assumed to have the same value as the corresponding steady-state interlaminar fracture toughness (which unlike the former, have well-established testing methods) - this assumption can be incorrect as the occurrence and extent of toughening mechanisms, such as fibre bridging, can largely vary in these different crack propagation directions. Therefore, this work aims to provide a novel and efficient three-dimensional (3D) micromechanical FE tool to estimate the mode I through-thickness intralaminar $\mathcal{R}$-curve of composite materials. A numerical framework is built for unstable crack propagation modelling, making use of the size effect method [18], having the advantages of: limiting the detailed region to a small embedded cell (EC) around the pre-crack tip; generating small virtual specimen geometries which are hard or even impossible to manufacture experimentally; and avoiding the necessity to track the position of the crack tip throughout the numerical simulations. The predictive capability of computational mechanics for heterogeneous materials largely depends on the scale at which damage is explicitly modelled [30, 31]. In particular, micromechanics can be used as a reliable tool for analysis and derivation of upscaled material properties in composite materials [32, 33, 34, 35, 36, 37]. Thus, with the appropriate constitutive material models and making use of unstable crack propagation virtual specimens, it is possible to better understand the mechanisms that underlie mode I through-thickness crack propagation in unidirectional fibre-reinforced composite materials.

2. Numerical framework

The 3D numerical framework is composed of different FE models of SENT specimens. They each consist of an EC, in which the inner structure of the material was modelled (fibres, matrix, and their interface), and of meso-scale parts that describe the homogenised behaviour of the micromechanical region. The EC is composed of several plies, each having a dispersion of fibres generated using a random distribution algorithm [38], embedded in an epoxy matrix and in fibre-matrix interfaces. The homogenised laminae behave linear-elastically and are connected to the EC by means of *Tie Constraints*. Figure 2 shows a front view of the EC and the surrounding homogenised regions. The following sub-sections report the constitutive material models and corresponding mechanical properties used to model each of the constituents and homogenised volume, as well as the FE framework used to conduct the numerical simulations.

[Figure 2 about here.]

2.1. Constitutive material models

At the micro-scale, mode I through-thickness intralaminar crack propagation mainly involves matrix and fibre-matrix interface related dissipation mechanisms. Consequently, the carbon fibres modelled here are considered to have a linear-elastic transversely isotropic behaviour. The geometry and material properties of the AS4 carbon fibres [39] are reported in Table 1.

[Table 1 about here.]

Since the Drucker-Prager or the Mohr-Coulomb models have been shown to perform poorly when modelling the behaviour of epoxy resins [28, 29], a more representative elasto-plastic damage constitutive material model, proposed by Melro et al. [40], was implemented as a VUMAT user subroutine in Abaqus®/Explicit [41]. To ensure consistency between the input and output fracture energies during damage localisation, a modification of the damage model was made following Arefi et al. [42].

Initially, the epoxy behaves elastically until a paraboloidal yield criterion is met [43]. In order to correctly define the plastic deformation under the presence of hydrostatic pressure, a non-associative flow rule is defined. The yield surface defined by the yield criterion depends only on the tensile and compressive yield strengths that are both affected by hardening, depending on the equivalent plastic strain, ε_e^p:

$$\varepsilon_e^p = \sqrt{\frac{1}{1+2\nu_p^2}\boldsymbol{\varepsilon^p} : \boldsymbol{\varepsilon^p}}, \tag{1}$$

with ν_p being the plastic Poisson's ratio of the matrix material and $\boldsymbol{\varepsilon^p}$ the plastic strain, in tensorial notation.

The degradation of the stiffness of the material is applied by using a damage model developed within the frameworks of the thermodynamics of admissible processes and uses a single damage variable, d^m. Damage onset is defined by the following damage activation function:

$$F_d^m = \phi_d^m - r^m = \frac{3\tilde{J}_2}{X_c^m X_t^m} + \frac{\tilde{I}_1(X_c^m - X_t^m)}{X_c^m X_t^m} - r^m, \tag{2}$$

where ϕ_d^m is the loading function, X_c^m and X_t^m respectively represent the compressive and tensile strengths of the material, and r^m is an internal variable relating to the matrix damage variable and it is given by:

$$r^m = \max\{1, \max_{t\to\infty}\{\phi_{d,t}^m\}\}. \tag{3}$$

Following [42], the invariants $\tilde{J}_2$ and $\tilde{I}_1$ are functions of the applied strain, ε_{22}:

$$\tilde{I}_1 = \frac{1}{(1-2\nu^m)(\varepsilon_f^m - \varepsilon_0^m)}\{\varepsilon_{22}[E^m(\varepsilon_f^m - \varepsilon_0^m) + 2\nu^m X_t^m] - 2\nu^m X_t^m \varepsilon_f^m\}, \tag{4a}$$

$$\tilde{J}_2 = \left(\frac{1}{(1+\nu^m)(\varepsilon_f^m - \varepsilon_0^m)}\{\varepsilon_{22}[E^m(\varepsilon_f^m - \varepsilon_0^m) - \nu^m X_t^m] + \nu^m X_t^m \varepsilon_f^m\}\right)^2, \tag{4b}$$

where ε_0^m and ε_f^m are the tensile initiation and failure strains of the matrix material under uniaxial tension, respectively. Since the constitutive material model incorporates plasticity, the value of the initiation strain is not simply given as $\varepsilon_0^m = X_t^m/E^m$. Therefore, the initiation strain is stored when the failure criterion presented in Equation (2) is verified. The failure strain is given as:

$$\varepsilon_f^m = \frac{2\mathcal{G}_{Ic}^m}{l_e^m X_t^m} + \varepsilon_e^p, \tag{5}$$

and the damage variable of the epoxy matrix is defined as [42]:

$$d^m = \frac{\varepsilon_f^m(\varepsilon_{22} - \varepsilon_0^m)}{\varepsilon_{22}(\varepsilon_f^m - \varepsilon_0^m)}. \tag{6}$$

By replacing the resultant loading function on the yield/damage surface [43], it is possible to derive the following expression for r^m, in terms of ε_{22}:

$$\varepsilon_{22} = \frac{\sqrt{q^2 - 4ps} - q}{2p}, \tag{7}$$

with:

$$q = 2b(1-b)c\varepsilon_f^m + (1+2b)d, \tag{8a}$$

$$p = c(1-b)^2, \tag{8b}$$

$$s = c(b\varepsilon_f^m)^2 - 2bd\varepsilon_f^m - r^m X_c^m X_t^m, \tag{8c}$$

$$b = \frac{\nu^m X_t^m}{E^m(\varepsilon_f^m - \varepsilon_0^m)}, \tag{8d}$$

$$c = \left(\frac{E^m}{1+\nu^m}\right)^2, \tag{8e}$$

$$d = \frac{E^m}{1-2\nu^m}(X_c^m - X_t^m). \tag{8f}$$

To avoid mesh size dependency, the characteristic element length, $l_e^m = \sqrt[3]{V_e^m}$ (where V_e^m represents the volume of the associated finite element), and the mode I steady-state fracture toughness of the epoxy, $\mathcal{G}_{Ic}^m$, were used to regularise the computed dissipated energy [44]. Due to the lack of a consideration of a material length, this formulation (*crack band model*) is local and under certain conditions it may not be the most appropriate one to model continuum damage [45]. However, as a consequence of the type of materials and stress-states considered here, the *crack band model* was deemed to be appropriate to model this type of crack propagation, since it ensures the correct energy dissipation in a localised damage band and it gives the correct transitional size effect [46].

The elastic and strength properties of the epoxy matrix considered here are the ones characterised by Ref. [35] for Hexcel 8552, through in-situ instrumented nanoindentation. Since the 8552 resin system cannot be easily obtained in a neat form, the mode I steady-state fracture toughness was obtained through experimental testing of a similar epoxy resin (Hexcel RTM6-2), using neat resin DENT specimens in combination with the size effect method. Pre-cracks for these specimens were introduced using the tapping method [47, 48]) in combination with the size effect method [18]. For the sake of brevity, only the final result obtained for the steady-state value of the mode I fracture toughness of the epoxy, $\mathcal{G}_{Ic}^m$, is reported here. Table 2 shows the mechanical properties of the considered 8552 epoxy system, including the $\mathcal{G}_{Ic}^{m}$ value obtained experimentally from the RTM6-2 epoxy.

[Table 2 about here.]

The fibre-matrix interface (FMI) was modelled using zero-thickness cohesive elements [49]. Damage onset was predicted using a quadratic stress failure criterion. The damage evolution law defined for interfacial damage propagation was assumed to be exponential [41]:

$$d^{\text{FMI}} = \int_{\delta_0^{\text{FMI}}}^{\delta_f^{\text{FMI}}} \frac{\sigma^{\text{FMI}}}{\mathcal{G}_c^{\text{FMI}} - \mathcal{G}_0^{\text{FMI}}} \, \mathrm{d}\delta^{\text{FMI}}, \tag{9}$$

where σ^{FMI} and δ^{FMI} are respectively, the interfacial effective traction and separation, δ_0^{FMI} and δ_f^{FMI} are respectively, the effective separation of the interface at damage initiation and complete failure [50]. $\mathcal{G}_0^{\text{FMI}}$ is the energy release rate at damage initiation, while $\mathcal{G}_c^{\text{FMI}}$ represents the fracture toughness of the fibre-matrix interface, that is evaluated according to the Benzeggagh-Kenane (BK) law [51], under mode I, mode II, and mixed mode (mode I + mode II). Table 3 shows the mechanical properties of the fibre-matrix interfaces considered in this work. Even though these interfacial parameters are hard to characterise, they are based on previous experimental observations [52, 53, 54] and computational micromechanical predictions [33, 34, 55, 56, 57].

[Table 3 about here.]

Since the homogenised regions of the FE framework are present only to reduce computational cost and to guarantee that the virtual specimens are sufficiently large to model the kinematics of a mode I unstable intralaminar characterisation test, they were modelled as linear-elastic, transversely isotropic with no damage. The elastic properties of these parts are here determined with parallel 3D micromechanical simulations using the concepts of Representative Volume Elements (RVEs), Periodic Boundary Conditions (PBCs), and volumetric homogenisation. The fibres are dispersed randomly in the RVE by making use of an already developed algorithm [58]. Following Melro et al. [59], the generated RVEs have in-plane and longitudinal dimensions of $30r$ and $4r$, respectively. Both constituents are modelled using C3D8R finite elements, with an average side length of 0.7 μm and constituent material properties from Tables 1 and 2. Table 4 shows the mean numerically predicted homogenised ply-level elastic properties of five different generated RVEs, having three fibre volume fractions, $\omega_f = 35\%$, $\omega_f = 56\%$, and $\omega_f = 71\%$, with different fibre distributions. The value of the homogenised density was obtained following Chamis' rule of mixtures.

[Table 4 about here.]

2.2. Finite element discretisation and boundary conditions

The micromechanical region is composed of a certain number of layers, as defined in sub-section 4.1, having a total width of w. Figure 3 shows a schematic representation of the SENT FE models, highlighting the EC and applied BCs. The vertical (x_2-direction) displacements of the bottom face of the model are blocked and a vertical tensile velocity-type BC is applied to the top face of the model. Each ply in the EC has a different random distribution of fibres [38] and a constant thickness of $w_p = 125$ μm. A resin-rich region, having a thickness of $\hat{w} = 4$ μm, is inserted between plies in order to model interlaminar regions. The total height of the ECs, l, was fixed for all models ($l = 500$ μm), thus, guaranteeing that damage propagates only due to the presence of the crack and not due to other features of the model. In the x_1-direction, the model assumes a state of plane strain, having a fixed dimension of $t = 750$ μm.

[Figure 3 about here.]

A pre-crack was inserted by deleting elements along the centreline of the EC to localise crack growth (see Figure 3). The pre-crack length in the EC (depicted in red in Figure 3) was chosen to be equal to the thickness of one ply, in order to ensure that onset and propagation of damage develops entirely within the EC. The total length of the FE models, $2L$, is equal to five times their total width ($2L = 5W$). The total length of the pre-crack was chosen to be $a_0 = W/2$ for all model configurations.

It has been shown that the steady-state value of the mode I longitudinal fibre-dominated intralaminar fracture toughness of UD [60] and 2D woven [22] composites is not significantly sensitive to the pre-crack tip radius of the unstable propagation specimens. By contrast, the experimental measurement of the mode I fracture toughness of brittle epoxies has been shown to exhibit a large dependency on this same pre-crack tip radius, due to the significantly smaller size of the FPZ of such epoxies, compared with fibre-reinforced composites. Consequently, different techniques of inducing pre-cracks generate different stress states and plastic regions ahead of the crack tip that yield different values of the measured fracture toughness [47, 48]. The numerical simulations were thus conducted using a pre-crack height which was approximately twice the size of the in-plane dimensions of the FE elements.

In the longitudinal direction, geometric variability should be assessed by incorporating fibre waviness, as done in Refs. [61, 62, 63, 64, 65]. However, the generation of such micromechanical imperfections is impractical due to the excessive computational cost, thus prohibiting the generation of FE models with a statistically significant number of fibres. Locally, the effectiveness of the matrix is affected by voidage, temperature variations, and variability in bulk resin content, amongst others [66, 67]. In an attempt to address such defects and longitudinal fibre misalignment, 3D variability is assessed by modifying the matrix and fibre-matrix interface corresponding strengths and fracture toughness, by multiplying them by a uniformly distributed scalar on the interval (0.7, 1.3). Consequently, the crack front will not grow uniformly along its thickness (x_1-direction), leading to tunnelling effects [68], thus enabling fibres to slightly bridge, obtaining a higher degree of crack tortuosity, and thus taking advantage of the 3D micromechanical framework. Following preliminary simulations, the use of the aforementioned uniformly distributed interval allowed for the fibres to bridge, whilst not greatly deviating from the reference property values.

All parts of the model were discretised with C3D8R finite elements, but the fibre-matrix interface that was modelled using COH3D8 zero-thickness finite elements. The EC and the homogenised volume have an average seed size of 0.8 μm and 2.5 μm, respectively. Moreover, a biased local seed size was inserted along the length (x_2-direction) of the homogenised volume, from 50 μm to 2000 μm. To avoid numerical errors induced by high element distortion, matrix and fibre-matrix interface elements having $d^m > 0.9999$ (Equation (6)) and $d^{\mathrm{FMI}} > 0.9999$ (Equation (9)), respectively, were deleted during the simulations.

Unstable crack growth occurs when the maximum load is reached, leading to the abrupt increase of the crack growth-rate and consequently of the local kinetic energy, invalidating quasi-static conditions [69, 70]. However, since the numerical framework makes sole use of the predictions obtained up to peak load, no extra considerations have to be undertaken in order to properly conduct such simulations.

3. Size effect method using SENT specimens

This section describes the size effect method proposed by Bažant [18] as a data reduction technique for unstable crack propagation testing.

The mode I through-thickness intralaminar $\mathcal{R}$-curve is here obtained by developing an analytical model based on Ref. [19]. For a 2D body, taking x_2 and x_3 as the two principal axis of the material (see Figures 2 and 3), the mode I energy release rate, $\mathcal{G}_I$, of a crack propagating parallel to the x_3-direction is given by:

$$\mathcal{G}_I = \frac{\mathcal{K}_I^2}{\acute{E}}, \tag{10}$$

where $\mathcal{K}_I$ is the mode I stress intensity factor and $\acute{E}$ is equal to the transverse or through-thickness Young's modulus ($\acute{E} = E_{22} = E_{33}$), respectively. Since the material is isotropic in the O_{23} plane, the stress intensity factor in Equation (10) is only a function of the shape and size of the specimen, and of the remote applied stress, σ [71]:

$$\mathcal{K}_I = \sigma\sqrt{W}\kappa(\alpha), \tag{11}$$

where $\kappa(\alpha)$ is a correction factor which depends on the non-dimensional parameter $\alpha = a/W$. Since the virtual specimens were subjected to a uniform remote displacement rather than stress, the correction factor was not calculated following analytical equations provided by, e.g. Tada et al. [72], but it was determined numerically following [19]. This was done by applying the Virtual Crack Closure Technique (VCCT) to a parametric FEM model, as done in literature [19, 20, 22]. Figure 4 shows the distribution of the correction factor, $\kappa(\alpha)$, for the virtual SENT specimens considered here.

[Figure 4 about here.]

The ultimate nominal stress, $\sigma_u = P_u/(tW)$, depends on the characteristic size of the specimen, W, following the size effect law of the material, $\sigma_u = \sigma_u(W)$.

The mode I critical strain energy release rate is obtained by observing that, at peak load, the crack driving force curve for each specimen size is tangential to the $\mathcal{R}$-curve at a unique point (see Figure 5):

$$\begin{cases} \mathcal{G}_I(\Delta a) &= \mathcal{R}(\Delta a) \\ \dfrac{\partial \mathcal{G}_I(\Delta a)}{\partial \Delta a} &= \dfrac{\partial \mathcal{R}(\Delta a)}{\partial \Delta a} \end{cases}. \tag{12}$$

[Figure 5 about here.]

Having prior knowledge of the size effect law of the material, $\sigma_u = \sigma_u(W)$, and substituting it into the first of Equation (12), it is possible to write [19]:

$$\mathcal{R}(\Delta a) = \frac{W\sigma_u^2}{\acute{E}}\kappa^2(\alpha_0 + \frac{\Delta a}{W}), \tag{13}$$

and by differentiating Equation (13) with respect to W, and recalling that the $\mathcal{R}$-curve is an intrinsic material property, the following equation is obtained:

$$\frac{\partial}{\partial W}(W\sigma_u^2\kappa^2) = 0. \tag{14}$$

By solving Equation (14) for $W = W(\Delta a)$, and then substituting W in Equation (13), the $\mathcal{R}$-curve is obtained [19].

Following Bažant and Planas [18], it is convenient to use one of the following analytical expressions for the size effect law: i) the linear regression I; ii) the linear regression II; or iii) the bilogarithmic regression. For the material analysed, the bilogarithmic regression law provided the best fit of the numerical data, using a non-linear least squares Levenberg-Marquardt optimisation:

$$\ln\,\sigma_u = \ln\,\frac{M}{\sqrt{N+W}}, \tag{15}$$

where M and N are the fitting parameters. The steady-state mode I intralaminar fracture toughness, and the fully developed length of the FPZ are respectively given by:

$$\mathcal{R}_{ss} = \frac{\kappa_0^2}{\acute{E}}M^2, \tag{16a}$$

$$l_{\mathrm{FPZ}} = \frac{\kappa_0}{2\acute{\kappa}_0}N, \tag{16b}$$

where $\kappa_0 = \kappa|_{\alpha=\alpha_0}$, and $\acute{\kappa}_0 = \mathrm{d}\kappa/\mathrm{d}\alpha|_{\alpha=\alpha_0}$.

4. Results

4.1. Effect of the size of the EC

Preliminary simulations were conducted to assess the influence of the number of layers of the EC on the peak load, P_u. Since SENT specimens own *positive geometry* (the crack driving force curve increases with the crack length), Equation (12) holds and the crack increment at the onset of unstable crack propagation should be, at most, equal to the fully developed length of the FPZ of the material, l_{FPZ}. Therefore, maintaining the width of the specimens equal to the maximum size that is meant to be analysed (i.e. $W = 30$ mm), where the crack extension before peak load will be largest, five different EC sizes were analysed, with increments of $2w_p$ (and $\hat{w}$) in the range of $2w_p \leqslant w \leqslant 10w_p$. Figure 6 shows the numerical predictions of the normalised load-displacement curves for different widths of the EC, where $\delta^c_{x_2}$ and $R^c_{x_2}$ respectively represent the critical applied displacement and reaction force, with $w = 8w_p$.

[Figure 6 about here.]

Only the ECs having $w \geqslant 8w_p$ yield a peak load, thus suggesting that the crack extension at instability is greater than $5w_p$. The peak load associated with the model having $w = 8w_p$ is approximately 3.6% higher that the one having $w = 10w_p$. Therefore, based on these results, in the following numerical analyses, a constant width of the EC of $w = 8w_p + 7\hat{w}$, is considered.

4.2. Effect of interfacial fracture toughness

The mechanical properties of the fibre-matrix interface are known to be extremely hard to characterise, especially the critical energy release rates. The single-fibre push-in test is a micromechanical experimental test which can be used to characterise the adhesion strength of a fibre-matrix interface [73, 74]. However, to the authors' best knowledge, there is no standard experimental technique to characterise the fracture toughness of the fibre-matrix interface. Therefore, a parametric study was here undertaken to assess the influence of the fibre-matrix interfacial fracture toughness on the estimated peak loads, and consequently on the $\mathcal{R}$-curve of the material. For a mode I crack propagating in the through-thickness direction (crack (iii) represented in Figure 1), the fibre-matrix interfacial debond growth occurs in mixed-mode loading conditions [57, 75]. Four cases were considered for this study, including one with no cohesive elements, and three with differing combinations of mode I and mode II interfacial fracture toughness values obtained from literature: i) $\mathcal{G}^{\mathrm{FMI}}_{Ic} = 0.002$ N/mm and $\mathcal{G}^{\mathrm{FMI}}_{IIc} = 0.006$ N/mm [33, 76, 77]; ii) $\mathcal{G}^{\mathrm{FMI}}_{Ic} = 0.020$ N/mm and $\mathcal{G}^{\mathrm{FMI}}_{IIc} = 0.050$ N/mm [78, 79, 80]; iii) $\mathcal{G}^{\mathrm{FMI}}_{Ic} = 0.125$ N/mm and $\mathcal{G}^{\mathrm{FMI}}_{IIc} = 0.150$ N/mm [27, 81, 82].

Figure 7 shows the numerical predictions of representative load-displacement curves for different W, for the same fibre distribution, with and without cohesive elements. Table 5 shows the numerical predictions of the mean peak loads and corresponding standard deviations of three different ECs for each size.

[Figure 7 about here.]

[Table 5 about here.]

As expected, the peak load increases with specimen size. However, this increase is not linearly proportional, confirming the presence of a size effect. In the post-peak response, after the crack has propagated unstably along the whole length of the EC, the homogenised linear-elastic volume is now carrying the load, justifying the rising part of the curve after instability. It is worth mentioning that, for the largest specimens, the predicted load-displacement curves are still linear up to failure, which is an indication of a "brittle" behaviour. However, in the FE models that made use of cohesive elements, the smaller specimen sizes deviated from the initial linear-elastic path before peak load, indicating a more quasi-brittle behaviour that deviates from simple LEFM predictions. Moreover, for the models having $\mathcal{G}_{Ic}^{\mathrm{FMI}} = 0.125$ N/mm (see Figure 7d), a significant amount of non-linearity was observed before unstable crack growth, also indicating a ductile behaviour caused by the excessive loading capacity of the fibre-matrix interfaces. The specimens having the biggest width, i.e. $W = 30$ mm and the toughest fibre-matrix interfaces, did not present a peak load due to the extremelly tough interfaces.

Using the values reported in Table 5 and a bilogarithmic regression fit (Equation (15)), the corresponding size effect laws, $\sigma_u = \sigma_u(W)$, are plotted in Figure 8.

[Figure 8 about here.]

The virtual testing of the different sized specimens capture the transition from the plastic limit behaviour, for the smaller specimens, to the bigger specimens characterised by LEFM [18, 71]. This transition can be observed in Figure 7b, where the smaller specimens ($W \leqslant 10$ mm) exhibit a non-linear behaviour before peak load, while for bigger specimens ($W \geqslant 15$ mm), the mechanical response is linear up to failure, which is in better agreement with LEFM. Figure 9 shows the normalised strength, σ_u/σ_0, and corresponding standard deviations, as a function of the normalised size, W/W_0, in double logarithmic scale, for the different fibre-matrix interface fracture toughness. W_0 and σ_0 represent size effect constants, while σ_u is given as:

$$\sigma_u = \frac{\sigma_0}{\sqrt{1 + W/W_0}}. \tag{17}$$

Equation (17) relates the nominal strength of the SENT scaled specimens to a characteristic size, describing the transition from ductile to brittle behaviour with increasing specimen size [18]. The results presented in Figure 9 show a transition from the strength criterion (plastic limit analysis), which is described by a horizontal asymptote, to an asymptote of slope $-1/2$, describing LEFM [18, 71].

[Figure 9 about here.]

Figures 10a-10d present the estimated $\mathcal{R}$-curves and corresponding 95% confidence intervals. Table 6 reports the predicted size effect fitting coefficients, M and N, the fully developed length of the FPZ, l_{FPZ}, and the steady-state value of the mode I through-thickness intralaminar fracture toughness, $\mathcal{R}_{ss}$. These $\mathcal{R}$-curves were obtained by using the crack driving force curves which where numerically-derived for different specimen sizes (in blue), including those which were specifically numerically tested (in red).

[Figure 10 about here.]

[Table 6 about here.]

Both l_{FPZ} and $\mathcal{R}_{ss}$ were observed to increase with higher interfacial fracture toughness, as observed experimentally by Montenegro et al. [83], in which tougher fibre-matrix interfaces led to an increase in the through-thickness steady-state fracture toughness.

The variation of $\mathcal{R}_{ss}$ with FMI fracture toughness is better depicted in Figure 11, including the corresponding 95% confidence intervals. The steady-state value of the mode I through-thickness fracture toughness estimated for the toughest fibre-matrix interface was expected to yield a broader 95% confidence interval, since only five different sized specimens produced peak loads for this specific FMI fracture toughness.

[Figure 11 about here.]

The steady-state fracture toughness obtained experimentally for similar thermoset CFRP composites [12] is between the steady-state values predicted here for mode I FMI fracture toughness of 0.020 N/mm and 0.125 N/mm. Comparing to the ones determined numerically by Ref. [26], for the same baseline properties, the framework presented in this paper yields a higher estimation of the $\mathcal{R}_{ss}$, this being attributed to the consideration of a 3D framework incorporating fibre bridging as an extra toughening mechanism. A similar comparison can be performed with the results obtained by Ref. [27] for glass fibre-reinforced polymers (GFRP), where for the same FMI fracture toughness ($\mathcal{G}_{Ic}^{\mathrm{FMI}} = 0.125$ N/mm and $\mathcal{G}_{IIc}^{\mathrm{FMI}} = 0.150$ N/mm) the present framework estimates, with 95% confidence, higher bounds of $\mathcal{R}_{ss}$ and l_{FPZ}.

From a qualitative point of view, Figure 12 shows the contour plots of the stress in the x_2-direction, σ_{22}, of different virtual specimens, evidencing the various stages of crack propagation, before (Figure 12a and Figure 12b) and after (Figure 12c) peak load. Matrix degradation, fibre-matrix interface debonding, and fibre bridging are the main sources of energy dissipation under this type of crack propagation. Small degrees of diffuse matrix damage (in small matrix cracks that extend outward of the principal one) can also occur, possibly leading to a slight overestimation of the mode I through-thickness intralaminar fracture toughness.

[Figure 12 about here.]

As it is shown in Figure 13, this framework is capable of exhibiting similar failure mechanisms as the experimental observations captured by scanning electron microscopies (SEMs) provided by Ref. [24].

[Figure 13 about here.]

Finally, Figure 14 shows an example of the failure pattern in the EC after unstable crack propagation, evidencing fibre bridging as a 3D toughening mechanism.

[Figure 14 about here.]

4.3. Effect of fibre volume fraction

This section aims to evaluate the effect of fibre volume fraction, ω_f, on the mode I through-thickness intralaminar $\mathcal{R}$-curve of the material having the previously reported fibre volume fractions (see Table 4).

Values of $\mathcal{G}_{Ic}^{\mathrm{FMI}} = 0.020$ N/mm and $\mathcal{G}_{IIc}^{\mathrm{FMI}} = 0.050$ N/mm were maintained constant for all simulations. For the sake of brevity, a smaller amount of results is presented.

Figure 15a shows one of the numerical predictions of the normalised load-displacement curves obtained for the three ω_f, for the same specimen width ($W = 20$ mm). As expected, the response of the material becomes stiffer when increasing fibre volume fraction. For the smallest fibre volume fraction ($\omega_f = 35\%$), as shown in Figure 15b, an increased amount of plasticity of the epoxy matrix could be noticed before crack propagation, followed by fibre-matrix debond propagation, possibly leading to a higher estimation of the failure displacement of the material. The increase of peak load reported by the model having the highest fibre volume fraction ($\omega_f = 71\%$) is due to the higher amount of fibre bridging, since there are more fibres inside the EC that can bridge (see Figure 15c).

[Figure 15 about here.]

The data reduction scheme presented in Section 3 was applied to the data obtained for the two other fibre volume fractions (see Table 4 for homogenised material properties). Figures 16a and 16b represent the normalised bar plots related to average peak loads and both $\mathcal{R}_{ss}$ and l_{FPZ}, respectively, associated to different ω_f. Since this type of failure mechanism is driven by fibre-matrix interface debonding, it is postulated that, for different interfacial mechanical properties, the ratio between the obtained results may differ.

[Figure 16 about here.]

Fibre volume fraction seems to play a role on the mode I through-thickness intralaminar $\mathcal{R}$-curve of the material, where both $\mathcal{R}_{ss}$ and l_{FPZ} increased with ω_f. To the best knowledge of the authors, there is no experimental evidence of the effect of the fibre volume fraction on this type of crack propagation. However, the effect of ω_f on the mode I and II interlaminar fracture toughness was studied by Refs. [84] and [85], respectively. For mode I interlaminar crack propagation, Ref. [84] concluded that increasing fibre volume fraction led to an increase in the steady-state value of the mode I interlaminar fracture toughness. This was mostly attributed to the increase of fibre bridging when increasing fibre volume fraction. Moreover, incrementing the fibre volume fraction (number of fibres per unit volume) leads to an increase of the tortuosity of the crack path. Since the actual length of the crack is larger than the equivalent length of the crack, the "apparent" fracture toughness increases. The higher tortuosity might also lead to more crack bridging depending on the strength and fracture toughness of the matrix and the interface, thus increasing even more the mode I through thickness intralaminar fracture toughness. By contrast, Ref. [85] reported a decrease in the fracture properties when increasing ω_f. The fracture surfaces near the insert region revealed a larger matrix-rich region in the low-fibre volume fraction composite, allowing for the development of a process zone that involved a higher degree of plasticity and cracking of the matrix constituent, thus leading to an increase in energy dissipation when comparing to high-fibre content composites.

5. Discussion and concluding remarks

The evaluation and proper characterisation of matrix-dominated intralaminar fracture toughness of composite materials needs to be improved, since it is a critical material parameter required for state-of-the art intralaminar damage models. However, the critical energy release rate for a slit matrix crack propagating in the "matrix-dominated" direction (cracks (i), (ii), (iii), and (iv) in Figure 1, respectively) is usually unavailable due to the lack of experimental test methods. Consequently, these are assumed to have the same value as the interlaminar fracture toughness (for the AS4/8552 UD composite material, the mode I interlaminar fracture toughness has been reported to be in the range of $[0.220, 0.320]$ N/mm [86, 87]), which are usually evaluated using standard test methods, such as the Double Cantilever Beam (DCB) [88] for mode I, the End Notch Flexure (ENF) [89] for mode II, and the Mixed Mode Bending (MMB) [90] for mixed-mode (mode I + mode II). This is commonly done, since both interlaminar and through-thickness/transverse intralaminar fracture mostly involve matrix plasticity and degradation, and fibre-matrix interfacial debonding. However, the toughening mechanism which determines the asymptotic value of the fracture toughness is fibre bridging. Even if fibre bridging still occurs in through-thickness/transverse intralaminar crack propagation, the occurrence of fibre bridging is most likely to be different amongst other crack propagation directions, possibly leading to dissimilar values of the fully developed length of the FPZ and steady-state fracture toughness, making it necessary to differentiate one type of crack propagation from the other [11].

The 3D micromechanical framework developed here is able to take into account certain mechanisms inherent to through-thickness intralaminar crack propagation. However, it is important to mention that there are certain drawbacks which were not assessed. Even if the damage model used here to model the matrix replicates the mechanical behaviour of an epoxy resin [40], it still represents a macromechanical damage model of a constituent. Chevalier et al. [91] concluded that macromechanical failure models used to model the behaviour of the constituents may promote premature failure of the material due to the excessive strain localisation in the epoxy matrix. Moreover, as it was estimated here, the numerically predicted steady-state fracture toughness is highly dependent on the fibre-matrix interface fracture toughness, making it crucial to develop experimental test methods to properly characterise the mechanical properties of such interfaces. Finally, damage of the fibrous reinforcements was not considered in this work, possibly leading to an overestimation of the predicted peak loads, during fibre bridging.

Despite the aforementioned pitfalls, the micromechanical framework developed here was able to successfully simulate mode I through-thickness intralaminar crack propagation through an efficient three-dimensional modelling strategy, capturing the main toughening mechanisms which underlie this type of crack growth in composite materials. Embedded cells were generated containing a random distribution of reinforcements [38], the epoxy matrix was modelled using an elasto-plastic damage model [40], and fibre-matrix interfaces were modelled using a cohesive zone model [49]. These detailed regions were connected to meso-scale parts in order to simulate the behaviour of single edge notch tension specimens, whose properties were obtained by conducting parallel micromechanical, linear-elastic numerical simulations, for different fibre volume fractions.

Summarising, with the present work, the following conclusions can be drawn:

- Preliminary results have shown that, to simulate an unstable intralaminar through-thickness crack propagation, the size of the EC has to be, at least, as long as the fully developed FPZ of the material.
- By generating different sizes of SENT virtual specimens and using the size effect method originally proposed by Bažant [18], it is possible to determine the crack resistance curves of the material. The transition from ductile to brittle behaviour with increasing specimen size was also observed [18, 71]. Fibre bridging is also a mechanism which was found to toughen the response and it can be captured using the three-dimensional framework presented here.
- Four different values of fibre-matrix interface fracture toughness were considered to assess their influence on the numerical prediction of the through-thickness $\mathcal{R}$-curve of the material. With increasing interfacial fracture toughness, both l_{FPZ} and $\mathcal{R}_{ss}$ increased as well, mostly due to the amount of crack shielding created by the tougher fibre-matrix interfaces, as seen experimentally [83].
- The effect of fibre volume fraction on the numerical predictions of the $\mathcal{R}$-curve was also a topic under study. It was seen that decreasing fibre volume fraction, the response becomes more non-linear due to the presence of matrix-rich regions. However, by contrast, increasing fibre volume fraction led to a higher prediction of the steady-state fracture toughness, a consequence of having more fibres inside the EC that can bridge, also leading to a higher degree of crack tortuosity, as seen experimentally by Ref. [84].
- Although a justification has been proposed here for the use of a fully 3D FE model, it should be noted that further scope for its use relies on the possibility of considering initial misalignment of the fibrous reinforcements, which can be modelled by using the algorithm proposed by Refs. [61, 64] that considers fibre misalignment as a stochastic process, as done by Ref. [65]. It is conceivable to postulate that this will further improve the accuracy of the proposed methodology.

In this work, computational micromechanics has been demonstrated to be an effective tool for assessing and understanding the mechanical behaviour of heterogeneous materials, giving more insight into the conditions governing mode I unstable crack propagation in a three-dimensional environment. Specimens which are hard to test physically were simulated, and the different micro-scale failure mechanisms were captured at a level which cannot be represented using meso- and/or macro-scale mechanical models.

Acknowledgements

The authors gratefully acknowledge the financial support of the project ICONIC – Improving the crashworthiness of composite transportation structures. ICONIC has received funding from the European Union's Horizon 2020 research and innovation programme under the Marie Skłodowska-Curie grant agreement No

721256. The content reflects only the author's view and the Agency is not responsible for any use that may be made of the information it contains. The second author would also like to acknowledge the project TEMPEST (H2020-WF-2018-2020), which received funding from the European Union's Horizon 2020 research and innovation programme under the grant agreement No 101038082.

Data availability

Datasets related to this article can be found at http://dx.doi.org/10.17632/z8x2hnpmhy.2, an open-source online data repository hosted at Mendeley Data.

References

[1] J. André Lavoie and Sotiris Kellas. Dynamic crush tests of energy-absorbing laminated composite plates. *Composites Part A: Applied Science and Manufacturing*, 27(6):467–475, 1996.

[2] A. G. Mamalis, D. E. Manolakos, G. A. Demosthenous, and M. B. Ioannidis. *Crashworthiness of Composite Thin-Walled Structures*. Taylor & Francis Routledge, 1st edition, 1998.

[3] O. Falcó, J.A. Mayugo, C.S. Lopes, N. Gascons, and J. Costa. Variable-stiffness composite panels: Defect tolerance under in-plane tensile loading. *Composites Part A: Applied Science and Manufacturing*, 63:21–31, aug 2014.

[4] Wei Tan, Brian G. Falzon, Louis N.S. Chiu, and Mark Price. Predicting low velocity impact damage and Compression-After-Impact (CAI) behaviour of composite laminates. *Composites Part A: Applied Science and Manufacturing*, 71:212–226, 2015.

[5] A. Soto, E.V. González, P. Maimí, F. Martín de la Escalera, J.R. Sainz de Aja, and E. Alvarez. Low velocity impact and compression after impact simulation of thin ply laminates. *Composites Part A: Applied Science and Manufacturing*, 109:413–427, jun 2018.

[6] I.R. Cózar, A. Turon, E.V. González, O. Vallmajó, and A. Sasikumar. A methodology to obtain material design allowables from high-fidelity compression after impact simulations on composite laminates. *Composites Part A: Applied Science and Manufacturing*, 139:106069, dec 2020.

[7] Zhibo Song, Shizhao Ming, Kaifan Du, Shaojun Feng, Caihua Zhou, Peng Hao, Shengli Xu, and Bo Wang. A novel equivalent method for crashworthiness analysis of composite tubes. *Composites Part A: Applied Science and Manufacturing*, 153:106761, feb 2022.

[8] L. Iannucci and M.L. Willows. An energy based damage mechanics approach to modelling impact onto woven composite materials: Part II. Experimental and numerical results. *Composites Part A: Applied Science and Manufacturing*, 38(2):540–554, feb 2007.

[9] Ireneusz Lapczyk and Juan A. Hurtado. Progressive damage modeling in fiber-reinforced materials. *Composites Part A: Applied Science and Manufacturing*, 38(11):2333–2341, nov 2007.

[10] P. Maimí, P.P. Camanho, J.A. Mayugo, and C.G. Dávila. A continuum damage model for composite laminates: Part I – Constitutive model. *Mechanics of Materials*, 39(10):897–908, 2007.

[11] F. Cepero, I.G. García, J. Justo, V. Mantič, and F. París. An experimental study of the translaminar fracture toughnesses in composites for different crack growth directions, parallel and transverse to the fiber direction. *Composites Science and Technology*, 181(February):107679, 2019.

[12] S. T. Pinho, P. Robinson, and L. Iannucci. Developing a four point bend specimen to measure the mode I intralaminar fracture toughness of unidirectional laminated composites. *Composites Science and Technology*, 69(7-8):1303–1309, 2009.

[13] S. T. Pinho, P. Robinson, and L. Iannucci. Fracture toughness of the tensile and compressive fibre failure modes in laminated composites. *Composites Science and Technology*, 66(13):2069–2079, 2006.

[14] Mauricio V. Donadon, Brian G. Falzon, Lorenzo Iannucci, and John M. Hodgkinson. Intralaminar toughness characterisation of unbalanced hybrid plain weave laminates. *Composites Part A: Applied Science and Manufacturing*, 38(6):1597–1611, 2007.

[15] Xiangqian Li, Stephen R. Hallett, Michael R. Wisnom, Navid Zobeiry, Reza Vaziri, and Anoush Poursartip. Experimental study of damage propagation in Over-height Compact Tension tests. *Composites Part A: Applied Science and Manufacturing*, 40(12):1891–1899, 2009.

[16] N. Blanco, D. Trias, S.T. Pinho, and P. Robinson. Intralaminar fracture toughness characterisation of woven composite laminates. Part II: Experimental characterisation. *Engineering Fracture Mechanics*, 131:361–370, 2014.

[17] H. Liu, B.G. Falzon, G. Catalanotti, and W. Tan. An experimental method to determine the intralaminar fracture toughness of high-strength carbon-fibre reinforced composite aerostructures. *The Aeronautical Journal*, 122(1255):1352–1370, sep 2018.

[18] Z. P. Bažant and J. Planas. *Fracture and Size Effect in Concrete and Other Quasibrittle Materials*. CRC Press, 1998.

[19] G. Catalanotti, A. Arteiro, M. Hayati, and P. P. Camanho. Determination of the mode I crack resistance curve of polymer composites using the size-effect law. *Engineering Fracture Mechanics*, 118:49–65, 2014.

[20] Marco Salviato, Kedar Kirane, Shiva Esna Ashari, Zdeněk P. Bažant, and Gianluca Cusatis. Experimental and numerical investigation of intra-laminar energy dissipation and size effect in two-dimensional textile composites. *Composites Science and Technology*, 135:67–75, 2016.

[21] R. F. Pinto, G. Catalanotti, and P. P. Camanho. Measuring the intralaminar crack resistance curve of fibre reinforced composites at extreme temperatures. *Composites Part A: Applied Science and Manufacturing*, 91:145–155, 2016.

[22] D. Dalli, G. Catalanotti, L.F. Varandas, B.G. Falzon, and S. Foster. Mode I intralaminar fracture toughness of 2D woven carbon fibre reinforced composites: A comparison of stable and unstable crack propagation techniques. *Engineering Fracture Mechanics*, 214:427–448, jun 2019.

[23] Seunghyun Ko, James Davey, Sam Douglass, Jinkyu Yang, Mark E. Tuttle, and Marco Salviato. Effect of the thickness on the fracturing behavior of discontinuous fiber composite structures. *Composites Part A: Applied Science and Manufacturing*, 125:105520, oct 2019.

[24] Luis Pablo Canal, Carlos González, Javier Segurado, and Javier LLorca. Intraply fracture of fiber-reinforced composites: Microscopic mechanisms and modeling. *Composites Science and Technology*, 72(11):1223–1232, 2012.

[25] D. J. Mortell, D. A. Tanner, and C. T. McCarthy. A virtual experimental approach to microscale composites testing. *Composite Structures*, 171:1–9, 2017.

[26] M. Herráez, C. González, and C. S. Lopes. A numerical framework to analyze fracture in composite materials: From R-curves to homogenized softening laws. *International Journal of Solids and Structures*, 134(November):216–228, 2018.

[27] Wei Tan and Emilio Martínez-Pañeda. Phase field predictions of microscopic fracture and R-curve behaviour of fibre-reinforced composites. *Composites Science and Technology*, 202:108539, jan 2021.

[28] M.N. Charalambides, A.J. Kinloch, and F.L. Matthews. Adhesively-bonded repairs to fibre-composite materials II. Finite element modelling. *Composites Part A: Applied Science and Manufacturing*, 29(11):1383–1396, nov 1998.

[29] Elhem Ghorbel. A viscoplastic constitutive model for polymeric materials. *International Journal of Plasticity*, 24(11):2032–2058, nov 2008.

[30] Pedro P. Camanho and Albertino Arteiro. Analysis Models for Polymer Composites Across Different Length Scales. In *The Structural Integrity of Carbon Fiber Composites*, pages 199–279. Springer International Publishing, 2017.

[31] Albertino Arteiro, Giuseppe Catalanotti, José Reinoso, Peter Linde, and Pedro P. Camanho. Simulation of the Mechanical Response of Thin-Ply Composites: From Computational Micro-Mechanics to Structural Analysis. *Archives of Computational Methods in Engineering*, sep 2018.

[32] T.J. Vaughan and C.T. McCarthy. A micromechanical study on the effect of intra-ply properties on transverse shear fracture in fibre reinforced composites. *Composites Part A: Applied Science and Manufacturing*, 42(9):1217–1228, sep 2011.

[33] A. R. Melro, P. P. Camanho, F. M. Andrade Pires, and S. T. Pinho. Micromechanical analysis of polymer composites reinforced by unidirectional fibres: Part II-Micromechanical analyses. *International Journal of Solids and Structures*, 50(11-12):1906–1915, 2013.

[34] A. Arteiro, G. Catalanotti, A. R. Melro, P. Linde, and P. P. Camanho. Micro-mechanical analysis of the effect of ply thickness on the transverse compressive strength of polymer composites. *Composites Part A: Applied Science and Manufacturing*, 79:127–137, 2015.

[35] F. Naya, C. González, C. S. Lopes, S. Van der Veen, and F. Pons. Computational micromechanics of the transverse and shear behavior of unidirectional fiber reinforced polymers including environmental effects. *Composites Part A: Applied Science and Manufacturing*, 92(June):146–157, 2017.

[36] L.F. Varandas, A. Arteiro, G. Catalanotti, and B.G. Falzon. Micromechanical analysis of interlaminar crack propagation between angled plies in mode I tests. *Composite Structures*, 220(December 2018):827–841, 2019.

[37] Mostafa Barzegar, Josep Costa, and Cláudio S. Lopes. High-fidelity computational micromechanics of first-fibre failure in unidirectional composites: Deformation mechanisms and stress concentration factors. *International Journal of Solids and Structures*, 204-205:18–33, nov 2020.

[38] L.F. Varandas, A. Arteiro, M.A. Bessa, A.R. Melro, and G. Catalanotti. The effect of through-thickness compressive stress on mode II interlaminar crack propagation: A computational micromechanics approach. *Composite Structures*, 182(September):326–334, 2017.

[39] P. D. Soden, M. J. Hinton, and A. S. Kaddour. Lamina properties, lay-up configurations and loading conditions for a range of fibre reinforced composite laminates. *Composites Science and Technology*, 58:30–51, 2004.

[40] A. R. Melro, P. P. Camanho, F. M. Andrade Pires, and S. T. Pinho. Micromechanical analysis of polymer composites reinforced by unidirectional fibres: Part I-Constitutive modelling. *International Journal of Solids and Structures*, 50(11-12):1897–1905, 2013.

[41] Dassault Systèmes, Providence, RI, USA. *ABAQUS Documentation.*

[42] Azam Arefi, Frans P. van der Meer, Mohammad Reza Forouzan, and Mohammad Silani. Formulation of a consistent pressure-dependent damage model with fracture energy as input. *Composite Structures*, 201(April):208–216, 2018.

[43] N. W. Tschoegl. Failure surfaces in principal stress space. *Journal of polymer science Part C: Polymer symposia*, 32(1):239–267, 1971.

[44] Z. Bažant and B. Oh. Crack band theory for fracture of concrete. *Materials and Structures*, 16:155–177, 1983.

[45] Zdeněk P. Bažant. Why continuum damage is nonlocal: Justification by quasiperiodic microcrack array. *Mechanics Research Communications*, 14(5-6):407–419, sep 1987.

[46] Zdeněk P. Bažant and Milan Jirásek. Nonlocal Integral Formulations of Plasticity and Damage: Survey of Progress. *Journal of Engineering Mechanics*, 128(11):1119–1149, nov 2002.

[47] A. B. Martínez, N. León, D. Arencón, J. Rodríguez, and A. Salazar. On the effect of the different notching techniques on the fracture toughness of PETG. *Polymer Testing*, 32(7):1244–1252, 2013.

[48] A. Salazar, J. Rodríguez, and A. B. Martínez. The role of notch sharpening on the J-fracture toughness of thermoplastic polymers. *Engineering Fracture Mechanics*, 101:10–22, 2013.

[49] A. Turon, P. P. Camanho, J. Costa, and C. G. Dávila. A damage model for the simulation of delamination in advanced composites under variable-mode loading. *Mechanics of Materials*, 38(11):1072–1089, 2006.

[50] P. Camanho and C.G. Davila. Mixed-Mode Decohesion Finite Elements for the Simulation of Delamination in Composite Materials. *NASA*, TM-2002-211737(June):1–37, 2002.

[51] M. L. Benzeggagh and M. Kenane. Measurement of mixed-mode delamination fracture toughness of unidirectional glass/epoxy composites with mixed-mode bending apparatus. *Composites Science and Technology*, 56(4):439–449, 1996.

[52] J. Varna, L. A. Berglund, and M. L. Ericson. Transverse single-fibre test for interfacial debonding in composites: 2. Modelling. *Composites Part A: Applied Science and Manufacturing*, 28(4):317–326, 1997.

[53] F. Naya, J. M. Molina-Aldareguía, C. S. Lopes, C. González, and J. Llorca. Interface Characterization in Fiber-Reinforced Polymer-Matrix Composites. *JOM*, 69(1):13–21, 2017.

[54] W. Tan, F. Naya, L. Yang, T. Chang, B. G. Falzon, L. Zhan, J. M. Molina-Aldareguía, C. González, and J. Llorca. The role of interfacial properties on the intralaminar and interlaminar damage behaviour of unidirectional composite laminates: Experimental characterization and multiscale modelling. *Composites Part B: Engineering*, 138(December 2017):206–221, 2018.

[55] Luís F. Varandas, Giuseppe Catalanotti, António R. Melro, and Brian G. Falzon. On the importance of nesting considerations for accurate computational damage modelling in 2D woven composite materials. *Computational Materials Science*, 172:109323, feb 2020.

[56] T. J. Vaughan and C. T. McCarthy. Micromechanical modelling of the transverse damage behaviour in fibre reinforced composites. *Composites Science and Technology*, 71(3):388–396, 2011.

[57] Linqi Zhuang, Ramesh Talreja, and Janis Varna. Transverse crack formation in unidirectional composites by linking of fibre/matrix debond cracks. *Composites Part A: Applied Science and Manufacturing*, 107(February):294–303, 2018.

[58] G. Catalanotti. On the generation of RVE-based models of composites reinforced with long fibres or spherical particles. *Composite Structures*, 138:84–95, 2016.

[59] A. R. Melro, P. P. Camanho, and S. T. Pinho. Influence of geometrical parameters on the elastic response of unidirectional composite materials. *Composite Structures*, 94(11):3223–3231, 2012.

[60] M. J. Laffan, S. T. Pinho, P. Robinson, and A. J. McMillan. Translaminar fracture toughness: The critical notch tip radius of 0° plies in CFRP. *Composites Science and Technology*, 72(1):97–102, 2011.

[61] G. Catalanotti and T. A. Sebaey. An algorithm for the generation of three-dimensional statistically Representative Volume Elements of unidirectional fibre-reinforced plastics : Focusing on the fibres waviness. *Composite Structures*, 227(July):111272, 2019.

[62] T.A. Sebaey, G. Catalanotti, and N.P. O'Dowd. A microscale integrated approach to measure and model fibre misalignment in fibre-reinforced composites. *Composites Science and Technology*, 183(August):107793, 2019.

[63] T.A. Sebaey, G. Catalanotti, C.S. Lopes, and N. O'Dowd. Computational micromechanics of the effect of fibre misalignment on the longitudinal compression and shear properties of UD fibre-reinforced plastics. *Composite Structures*, 248:112487, sep 2020.

[64] G. Catalanotti, L.F. Varandas, António R. Melro, T.A. Sebaey, M.A. Bessa, and B.G. Falzon. Modelling the longitudinal failure of fibre-reinforced composites at microscale. In *Multi-Scale Continuum Mechanics Modelling of Fibre-Reinforced Polymer Composites*, pages 349–378. Elsevier, 2021.

[65] L. F. Varandas, G. Catalanotti, A. R. Melro, R. P. Tavares, and B. G. Falzon. Micromechanical modelling of the longitudinal compressive and tensile failure of unidirectional composites: The effect of

fibre misalignment introduced via a stochastic process. *International Journal of Solids and Structures*, 203:157–176, 2020.

[66] M.R. Wisnom, M. Gigliotti, N. Ersoy, M. Campbell, and K.D. Potter. Mechanisms generating residual stresses and distortion during manufacture of polymer–matrix composite structures. *Composites Part A: Applied Science and Manufacturing*, 37(4):522–529, apr 2006.

[67] K. Potter. Manufacturing defects as a cause of failure in polymer matrix composites. *Failure Mechanisms in Polymer Matrix Composites: Criteria, Testing and Industrial Applications*, pages 26–52, 2012.

[68] M.A James and J.C Newman. The effect of crack tunneling on crack growth: experiments and CTOA analyses. *Engineering Fracture Mechanics*, 70(3-4):457–468, feb 2003.

[69] Yu. G. Matvienko. Crack growth in the process of unstable brittle fracture. *Materials Science*, 32(6):724–729, nov 1996.

[70] Chih-Hung Chen, Eran Bouchbinder, and Alain Karma. Instability in dynamic fracture and the failure of the classical theory of cracks. *Nature Physics*, 13(12):1186–1190, dec 2017.

[71] Zdenek P. Bažant, Isaac M. Daniel, and Zhengzhi Li. Size effect and fracture characteristics of composite laminates. *Journal of Engineering Materials and Technology, Transactions of the ASME*, 118(3):317–324, 1996.

[72] Hiroshi Tada, Paul C. Paris, and George R. Irwin. *The Stress Analysis of Cracks Handbook*. 1973.

[73] M. Kharrat, A. Chateauminois, L. Carpentier, and P. Kapsa. On the interfacial behaviour of a glass/epoxy composite during a micro-indentation test: Assessment of interfacial shear strength using reduced indentation curves. *Composites Part A: Applied Science and Manufacturing*, 28(1):39–46, 1997.

[74] M. Rodríguez, J. M. Molina-Aldareguía, C. González, and J. Llorca. A methodology to measure the interface shear strength by means of the fiber push-in test. *Composites Science and Technology*, 72(15):1924–1932, 2012.

[75] Luca Di Stasio, Janis Varna, and Zoubir Ayadi. Energy release rate of the fiber/matrix interface crack in UD composites under transverse loading: Effect of the fiber volume fraction and of the distance to the free surface and to non-adjacent debonds. *Theoretical and Applied Fracture Mechanics*, 103(April), 2019.

[76] A. Arteiro, G. Catalanotti, A. R. Melro, P. Linde, and P. P. Camanho. Micro-mechanical analysis of the in situ effect in polymer composite laminates. *Composite Structures*, 116(1):827–840, 2014.

[77] D. Garoz, F. A. Gilabert, R. D.B. Sevenois, S. W.F. Spronk, and W. Van Paepegem. Consistent application of periodic boundary conditions in implicit and explicit finite element simulations of damage in composites. *Composites Part B: Engineering*, 168(December 2018):254–266, 2019.

[78] W. Steenstra, F. P. van der Meer, and L. J. Sluys. An efficient approach to the modeling of compressive transverse cracking in composite laminates. *Composite Structures*, 128:115–121, 2015.

[79] Frans P. van der Meer, Sibrand Raijmaekers, and Iuri B.C.M. Rocha. Interpreting the single fiber

fragmentation test with numerical simulations. *Composites Part A: Applied Science and Manufacturing*, 118:259–266, mar 2019.

[80] Y. Liu, F.P. van der Meer, L.J. Sluys, and L. Ke. Modeling of dynamic mode I crack growth in glass fiber-reinforced polymer composites: fracture energy and failure mechanism. *Engineering Fracture Mechanics*, 243:107522, feb 2021.

[81] Ganesh Soni, Ramesh Singh, Mira Mitra, and Brian G. Falzon. Modelling matrix damage and fibre-matrix interfacial decohesion in composite laminates via a multi-fibre multi-layer representative volume element (M2RVE). *International Journal of Solids and Structures*, 51(2):449–461, 2014.

[82] D. Esqué-De Los Ojos, R. Ghisleni, A. Battisti, G. Mohanty, J. Michler, J. Sort, and A. J. Brunner. Understanding the mechanical behavior of fiber/matrix interfaces during push-in tests by means of finite element simulations and a cohesive zone model. *Computational Materials Science*, 117:330–337, 2016.

[83] Davi M. Montenegro, Francesco Bernasconi, Markus Zogg, Matthias Gössi, Rafael Libanori, Konrad Wegener, and André R. Studart. Mode I transverse intralaminar fracture in glass fiber-reinforced polymers with ductile matrices. *Composite Structures*, 165:65–73, 2017.

[84] P. Compston and P. Y.B. Jar. Influence of fibre volume fraction on the mode I interlaminar fracture toughness of a glass-fibre/vinyl ester composite. *Applied Composite Materials*, 6(6):353–368, 1999.

[85] Peter Davies, P. Casari, and L. A. Carlsson. Influence of fibre volume fraction on mode II interlaminar fracture toughness of glass/epoxy using the 4ENF specimen. *Composites Science and Technology*, 65(2):295–300, 2005.

[86] J. Renart, N. Blanco, E. Pajares, J. Costa, S. Lazcano, and G. Santacruz. Side Clamped Beam (SCB) hinge system for delamination tests in beam-type composite specimens. *Composites Science and Technology*, 71(8):1023–1029, 2011.

[87] V. Mollón, J. Bonhomme, A. M. Elmarakbi, A. Argüelles, and J. Viña. Finite element modelling of mode I delamination specimens by means of implicit and explicit solvers. *Polymer Testing*, 31(3):404–410, 2012.

[88] ASTM D5528-13. ASTM D5528-13, Standard Test Method for Mode I Interlaminar Fracture Toughness of Unidirectional Fiber-Reinforced Polymer Matrix Composites, 2013.

[89] ASTM D7905. ASTM D7905 / D7905M-14, Standard Test Method for Determination of the Mode II Interlaminar Fracture Toughness of Unidirectional Fiber-Reinforced Polymer Matrix Composites, 2014.

[90] ASTM D6671. ASTM D6671 / D6671M-19, Standard Test Method for Mixed Mode I-Mode II Interlaminar Fracture Toughness of Unidirectional Fiber Reinforced Polymer Matrix Composites, 2019.

[91] J. Chevalier, P. P. Camanho, F. Lani, and T. Pardoen. Multi-scale characterization and modelling of the transverse compression response of unidirectional carbon fiber reinforced epoxy. *Composite Structures*, 209(July 2018):160–176, 2019.

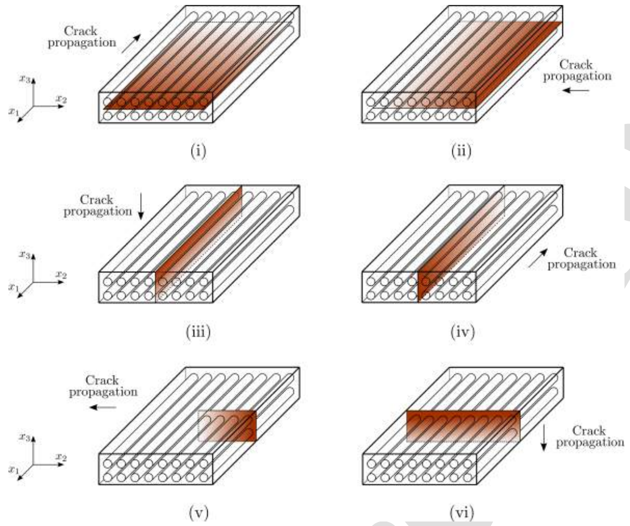

Figure 1: Schematic representation of different types of intralaminar crack propagation, mainly promoting a higher degree of matrix cracking, fibre-matrix interface debonding, and fibre bridging (cracks (i), (ii), (iii), and (iv)), or fibre breakage as a main toughening mechanism (cracks (v) and (vi)).

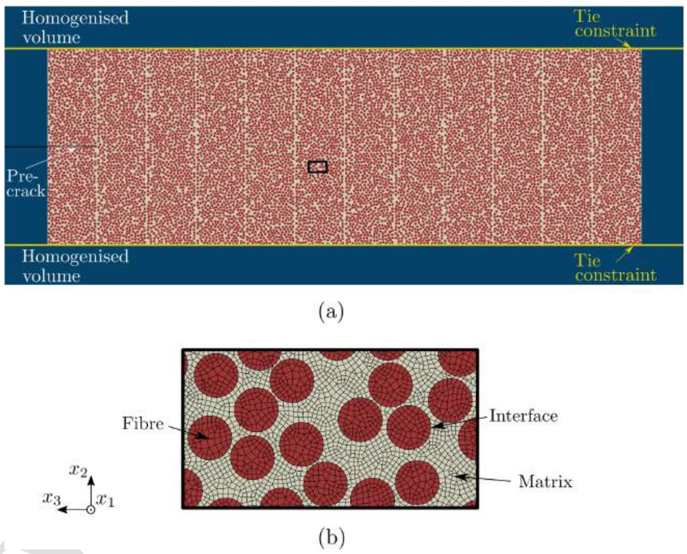

Figure 2: (a) Front view of the micromechanical region and homogenised outer plies; (b) zoomed image of the EC, highlighting the mesh density. White - matrix; red - fibres; blue - homogenised volume.

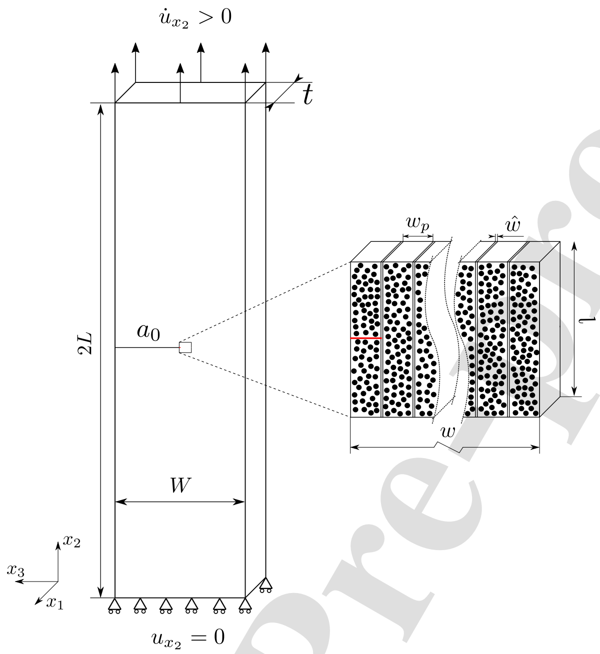

Figure 3: Schematic representation of the FE SENT models, highlighting the region of the EC and the BCs applied to the model. The pre-crack is depicted in red.

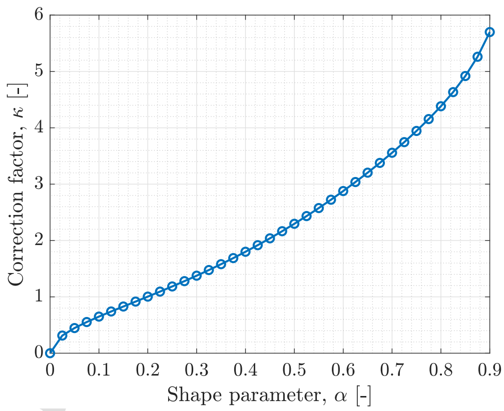

Figure 4: Variation of the correction factor, κ, with the shape parameter, α.

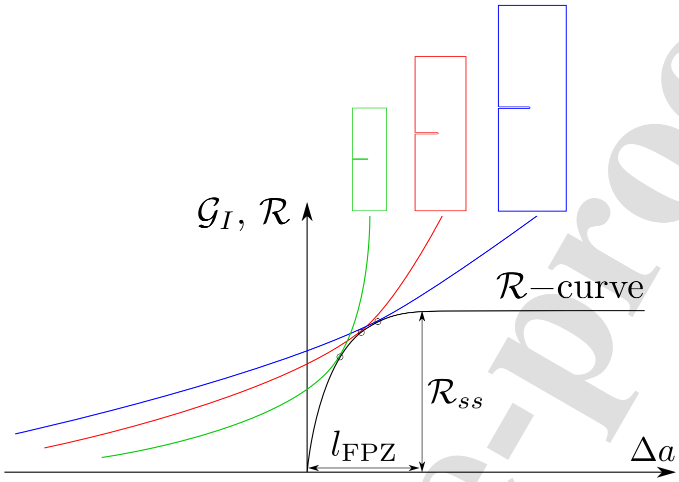

Figure 5: Representation of driving force curves for different scaled SENT specimens and $\mathcal{R}$-curve.

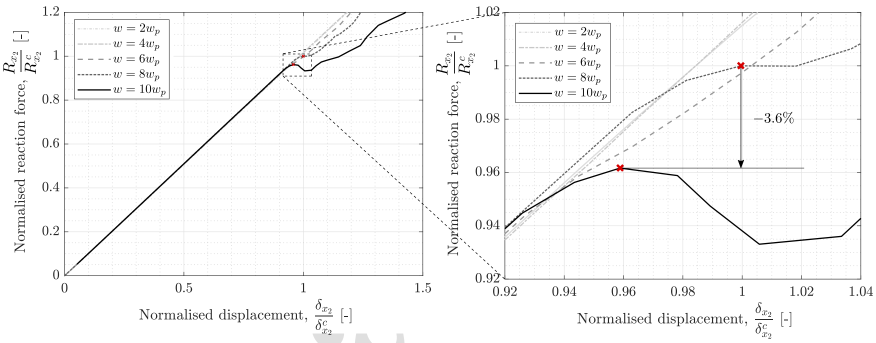

Figure 6: Normalised load-displacement curves for different w, maintaining $W = 30$ mm.

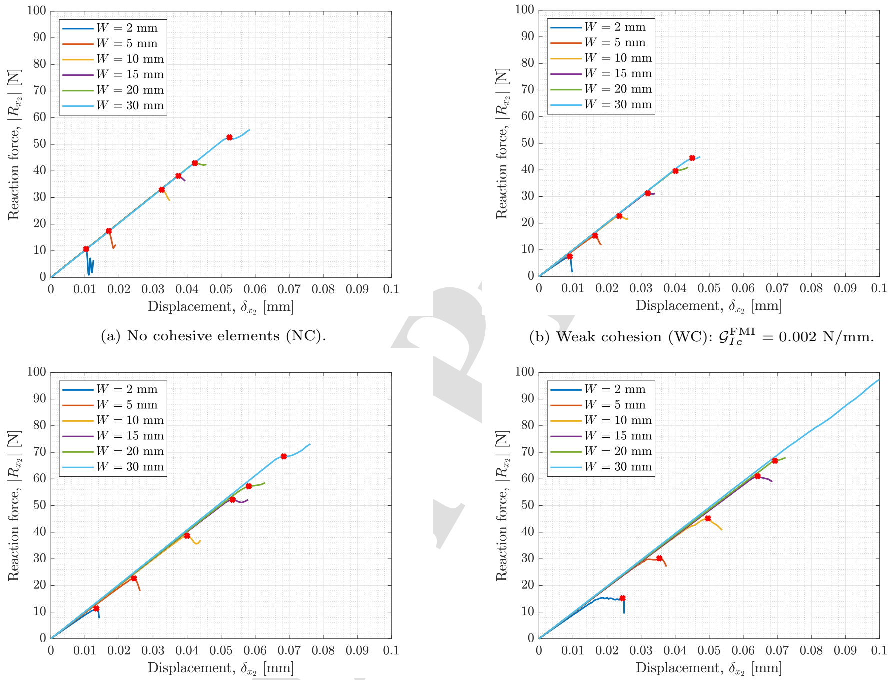

(a) No cohesive elements (NC).

(b) Weak cohesion (WC): $\mathcal{G}_{Ic}^{\text{FMI}} = 0.002$ N/mm.

(c) Medium cohesion (MC): $\mathcal{G}_{Ic}^{\text{FMI}} = 0.020$ N/mm.

(d) Strong cohesion (SC): $\mathcal{G}_{Ic}^{\text{FMI}} = 0.125$ N/mm.

Figure 7: Numerical predictions of representative load-displacement curves for different specimen widths, for the same fibre distribution and different fibre-matrix interface fracture toughness. The red crosses indicate the peak loads.

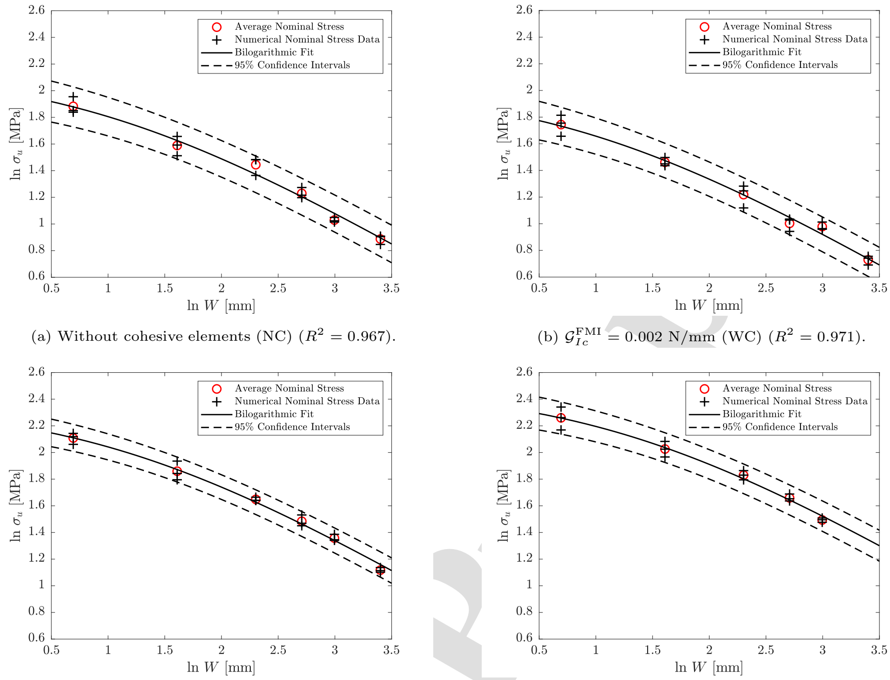

(a) Without cohesive elements (NC) ($R^2 = 0.967$).

(b) $\mathcal{G}_{Ic}^{\text{FMI}} = 0.002$ N/mm (WC) ($R^2 = 0.971$).

(c) $\mathcal{G}_{Ic}^{\text{FMI}} = 0.020$ N/mm (MC) ($R^2 = 0.984$).

(d) $\mathcal{G}_{Ic}^{\text{FMI}} = 0.125$ N/mm (SC) ($R^2 = 0.969$).

Figure 8: Bilogarithmic size effect regression curves for different values of fibre-matrix interface fracture toughness.

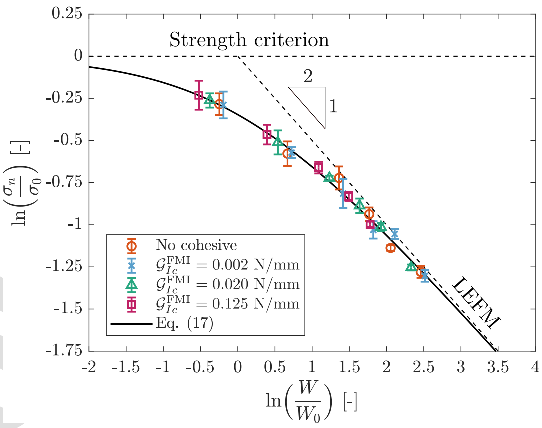

Figure 9: Numerical predictions of the normalised strength-characteristic size in double logarithmic scale.

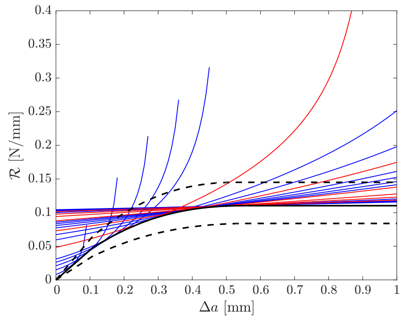

(a) Without cohesive elements (NC).

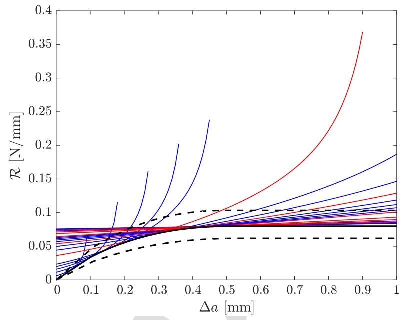

(b) $\mathcal{G}_{Ic}^{\mathrm{FMI}} = 0.002$ N/mm (WC).

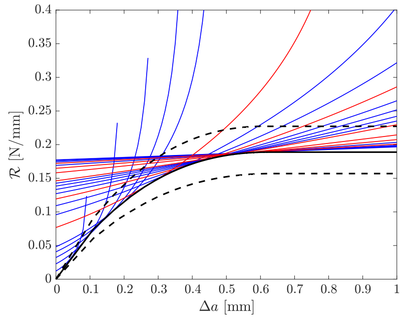

(c) $\mathcal{G}_{Ic}^{\mathrm{FMI}} = 0.020$ N/mm (MC).

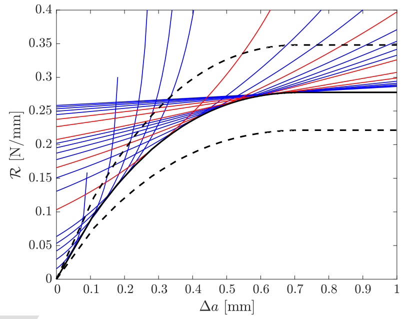

(d) $\mathcal{G}_{Ic}^{\mathrm{FMI}} = 0.125$ N/mm (SC).

Figure 10: Estimated $\mathcal{R}$-curves of the material (in black) with 95% confidence limits (in dashed black), together with individual $\mathcal{G}_I(\Delta a)$ curves for different-sized SENT specimens (blue), including the sizes modelled in this study (red).

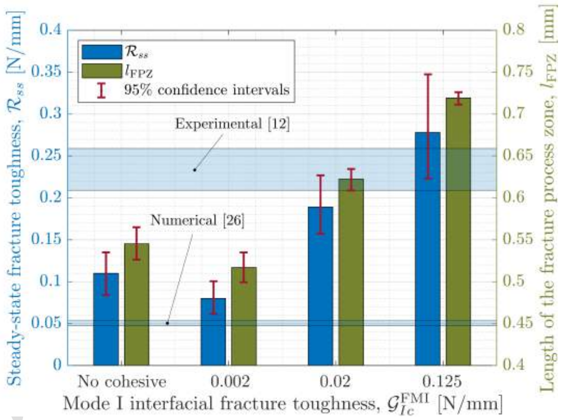

Figure 11: Bar charts showing the numerical predictions of $\mathcal{R}_{ss}$ and l_{FPZ} vs. FMI fracture toughness, including the corresponding 95% confidence intervals as error bars. Both experimental [12] and numerical [26] estimations of the steady-state through-thickness/transverse intralaminar fracture toughness for CFRPs are included as reference.

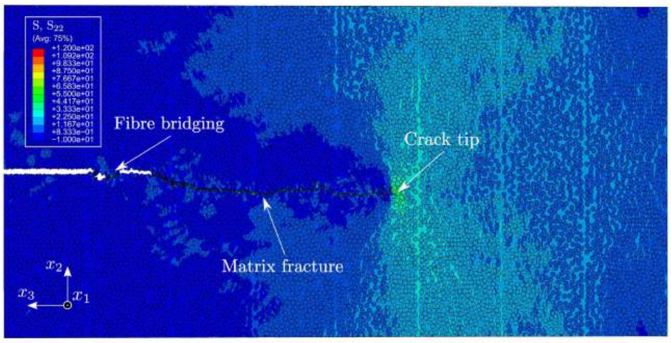

(a)

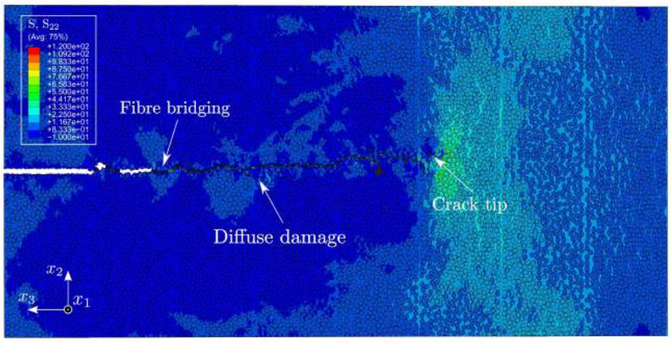

(b)

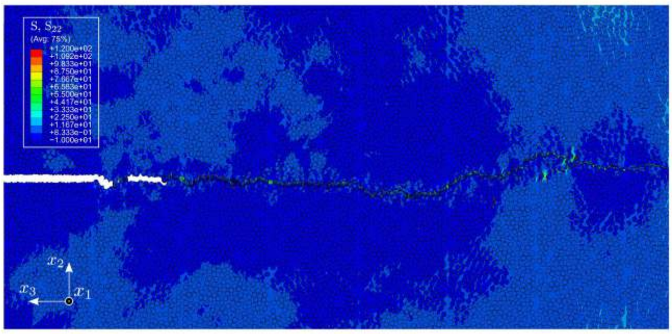

(c)

Figure 12: Contour plots of the transverse stress, σ_{22} (in MPa), for virtual specimens having different characteristic sizes. (a) and (b): Before peak load; (c): After peak load.

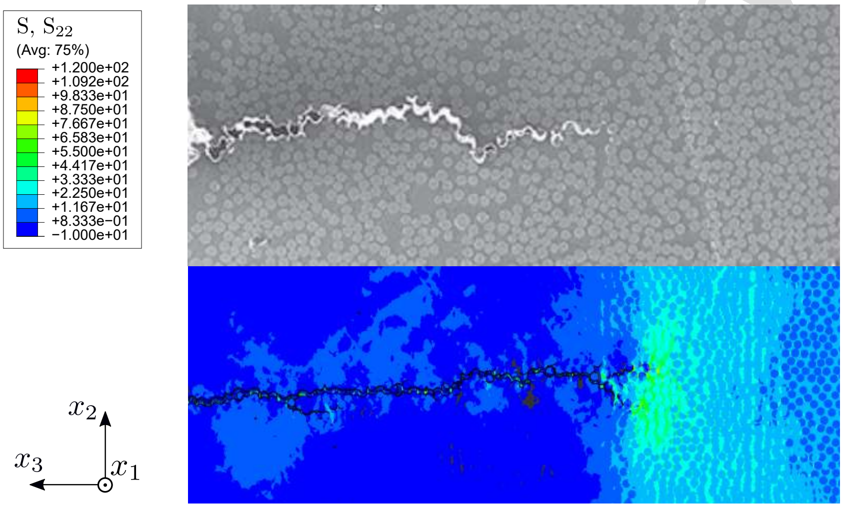

(a) Example #1.

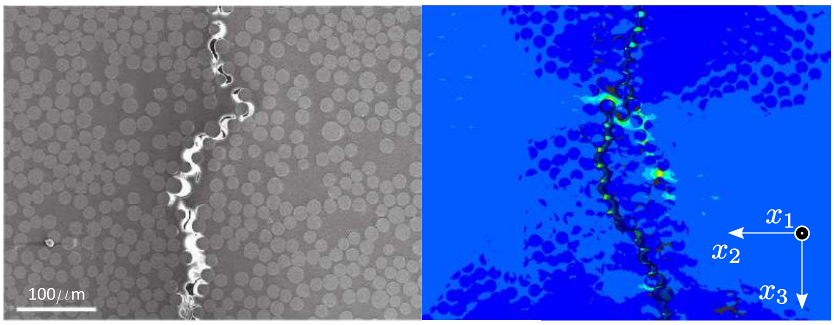

(b) Example #2.

Figure 13: Contour plots of the transverse stress σ_{22} (in MPa - same limits for both figures) in comparison to the experimental SEM results (in grayscale) provided by Ref. [24] (with permission).

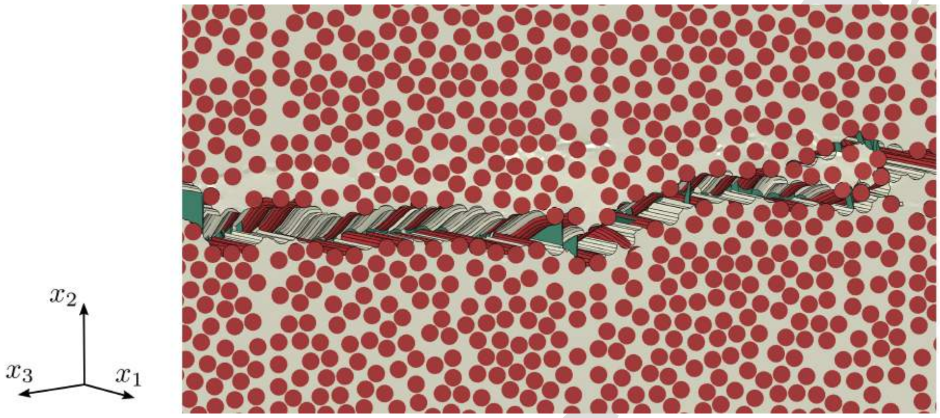

Figure 14: Bridging area after unstable crack propagation. White - matrix; red - fibres; green - fibre-matrix interfaces.

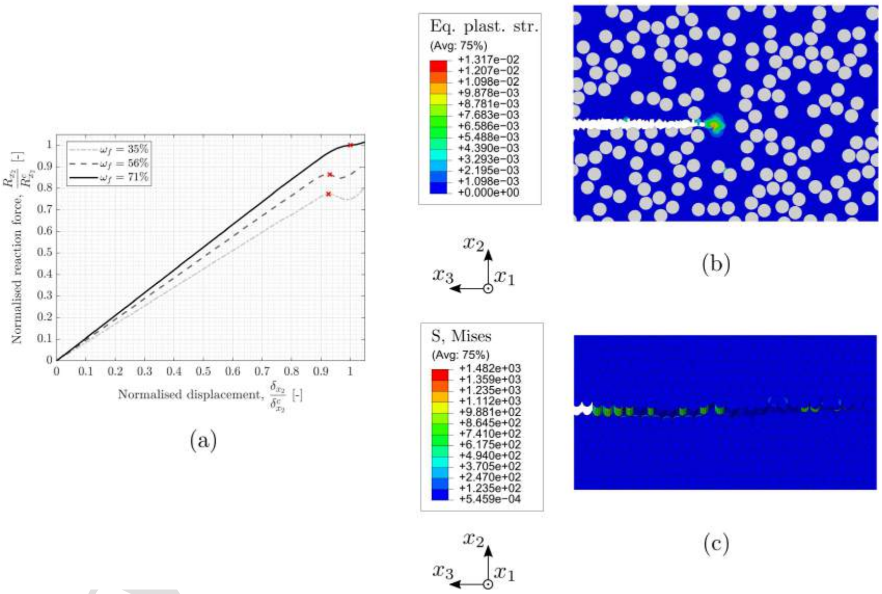

Figure 15: (a) Quantitative predictions of the normalised load-displacement curves for the three different fibre volume fractions, having the same characteristic size, $W = 20$ mm. (b) and (c) Contour plots of the equivalent plastic strain (Equation (1)), and von Mises stress considering $\omega_f = 35\%$ and $\omega_f = 71\%$, respectively.

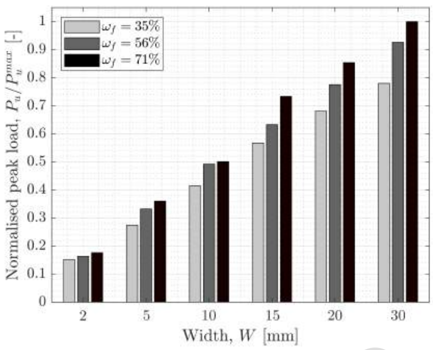

(a) Normalised peak loads vs. specimen width.

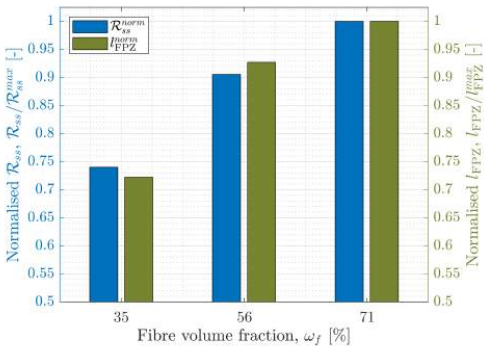

(b) $\mathcal{R}_{ss}^{norm}$ and $l_{\mathbf{FPZ}}^{norm}$.

Figure 16: Bar charts covering normalised predictions obtained for different fibre volume fractions, ω_f.

Table 1: AS4 carbon fibre properties [39].

Material property	Value
Fibre radius	
r [μm]	3.5
Young's moduli	
E_{11}^{f} [GPa]	225
E_{22}^{f} [GPa]	15
In-plane Poisson's ratio	
ν_{12}^{f} [-]	0.2
Shear moduli	
G_{12}^{f} [GPa]	15
G_{23}^{f} [GPa]	7
Density	
ρ^{f} [kg/mm^3]	1.78×10^{-6}

Table 2: Matrix material properties [33, 35].

Material property	Value
Young's modulus	
E^{m} [GPa]	5.07
Poisson's ratio	
ν^{m} [-]	0.35
Plastic Poisson's ratio	
ν_{p}^{m} [-]	0.30
Tensile strength	
X_{t}^{m} [MPa]	121
Compressive strength	
X_{c}^{m} [MPa]	180
Mode I fracture toughness	
$\mathcal{G}_{Ic}^{m}$ [N/mm]	0.13
Density	
ρ^{m} [kg/mm^3]	1.30×10^{-6}

Table 3: Fibre-matrix interface properties [33, 34, 52].

Material property	Value
Interface stiffness	
K [N/mm^3]	10^6
Interface strengths	
τ_1^0 [MPa]	75
τ_2^0 [MPa]	75
τ_3^0 [MPa]	50
Mixed-mode interaction parameter (BK law [51])	
η	1.45

Table 4: Homogenised properties of the meso-scale volumes.

Material property	$\omega_f = 35\%$	$\omega_f = 56\%$	$\omega_f = 71\%$
Young's moduli			
E_{11} [GPa]	84.1	130.3	160.9
E_{22} [GPa]	8.2	9.4	10.3
Poisson's ratios			
ν_{12} [-]	0.39	0.32	0.27
ν_{23} [-]	0.46	0.38	0.29
In-plane shear modulus			
G_{12} [GPa]	3.9	4.8	6.1
Density			
ρ [kg/mm^3]	1.47×10^{-6}	1.57×10^{-6}	1.64×10^{-6}

Table 5: Numerical predictions of the corresponding mean peak load, P_u^{med}, and their standard deviation (in {} brackets) for models having no cohesive (NC) elements and having cohesive elements with a weak cohesion - WC ($\mathcal{G}_{Ic}^{\text{FMI}} = 0.002$ N/mm), medium cohesion - MC ($\mathcal{G}_{Ic}^{\text{FMI}} = 0.020$ N/mm), and strong cohesion - SC ($\mathcal{G}_{Ic}^{\text{FMI}} = 0.125$ N/mm).

Width, W [mm]	NC [N]	WC [N]	MC [N]	SC [N]
2	9.857 {0.640}	8.579 {0.675}	12.353 {0.517}	14.372 {1.230}
5	18.368 {1.327}	16.164 {0.528}	24.078 {1.734}	28.438 {1.658}
10	31.803 {2.127}	25.361 {2.134}	38.993 {0.548}	46.755 {1.615}
15	38.472 {1.550}	30.660 {1.550}	49.628 {2.124}	59.140 {1.576}
20	41.989 {0.758}	39.910 {1.202}	58.303 {1.464}	66.790 {1.071}
30	54.633 {1.882}	46.671 {1.588}	68.790 {1.208}	$---$ {$---$}

Table 6: Estimated size effect law fitting coefficients (M and N), fully developed length of the FPZ (l_{FPZ}) and steady-state fracture toughness ($\mathcal{R}_{ss}$) for different FMI fracture toughness: no cohesion - NC; weak cohesion - WC ($\mathcal{G}_{Ic}^{\text{FMI}} = 0.002$ N/mm); medium cohesion - MC ($\mathcal{G}_{Ic}^{\text{FMI}} = 0.020$ N/mm); and strong cohesion - SC ($\mathcal{G}_{Ic}^{\text{FMI}} = 0.125$ N/mm).

FMI	M [MPa$\sqrt{\text{mm}}$]	N [mm]	l_{FPZ} [mm]	$\mathcal{R}_{ss}$ [N/mm]
NC	13.978	2.562	0.546	0.110
WC	11.895	2.425	0.517	0.080
MC	18.291	2.917	0.622	0.189
SC	22.179	3.374	0.719	0.278

- Micromechanical models were built to investigate intralaminar failure of composites.
- The size effect method was applied as a data reduction technique.
- The size-dependent transition in quasi-brittle behaviour was captured.
- Tougher fibre-matrix interfaces led to an increased composite fracture toughness.
- Fibre volume fraction played a role on the estimation of the intralaminar $\mathcal{R}$-curve.

Credit Author Statement

L. F. Varandas: Conceptualisation, Methodology, Software, Validation, Formal Analysis, Investigation, Data curation, Writing - original draft, Writing - review & editing, Visualisation.

D. Dalli: Conceptualisation, Methodology, Software, Validation, Formal Analysis, Writing - original draft, Writing - review & editing, Visualisation.

G. Catalanotti: Conceptualisation, Resources, Methodology, Software, Formal Analysis, Writing - review & editing, Supervision.

B. G. Falzon: Conceptualisation, Resources, Writing - review & editing, Supervision, Funding acquisition.

Declaration of interests

☒ The authors declare that they have no known competing financial interests or personal relationships that could have appeared to influence the work reported in this paper.

☐ The authors declare the following financial interests/personal relationships which may be considered as potential competing interests: